Viscous drag force model for dynamic Wilhelmy plate experiments

Peter Zhang
Department of Mechanical and Aerospace Engineering, University of Florida, Gainesville, Florida 32611, USA

Kamran Mohseni*
Department of Mechanical and Aerospace Engineering, University of Florida, Gainesville, Florida 32611, USA
and Department of Electrical and Computer Engineering, University of Florida, Gainesville, Florida 32611, USA

(Received 2 May 2019; published 21 August 2019)

In this work we revisit the dynamic Wilhelmy plate method for measuring dynamic contact angles with a specific focus on the viscous drag force which acts along the submerged surface of the plate. Particle image velocimetry shows that the viscous drag force can induce significant contact angle measurement errors if ignored. Preexisting models are found to underestimate the viscous drag force at moderate to high Capillary numbers, in finite-sized fluid domains, and for curved interfaces. Therefore, we propose a new model for the shear stress along a Wilhelmy plate by combining the dominant terms from a moving contact line flow, a Stokes flow past the leading edge of a flat plate, and a Couette-Poiseuille flow. This new model accounts for the shape of the fluid interface, the finite length of the plate, and the finite-size of the fluid container. Good agreement is obtained in comparisons with particle image velocimetry measurements over a Capillary number range from 0.001 to 0.3. This viscous drag model is applied to a dynamic Wilhelmy plate experiment and we obtain dynamic microscopic contact angle measurements and unbalanced Young's forces that are consistent with hydrodynamic theories of the moving contact line.

DOI: 10.1103/PhysRevFluids.4.084004

I. INTRODUCTION

For decades wetting and dewetting has been a topic of significant interest to the scientific community due to the wide range of fascinating phenomena associated with the contact line. While small in size, the moving contact line (MCL) has a significant effect on many natural and industrial problems including drop impact [1], boiling [2], coatings [3], and inkjet printing [4], among others [5–10]. In the study of contact lines, the contact angle is often the parameter of interest and most MCL models have focused on determining how the dynamic contact angle changes as a function of Capillary number [11–16]. However, modeling and measuring the dynamic contact angle has proven to be a challenging task as it is a sensitive parameter that also depends on length scale [17].

In the case of static contact angles, a variety of measurement methods have been developed and they can be broadly classified as optical or force based methods. Optical methods take highly magnified images and measure the contact angle between a tangent line fitted to the fluid interface and the solid surface. Optical methods are advantageous because they are relatively simple, require

*mohseni@ufl.edu

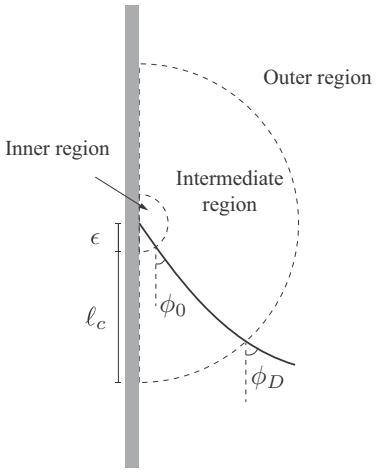

FIG. 1. Schematic of the interface shape near a moving contact line. The microscopic contact angle ϕ_0 is measured at a distance ϵ from the contact line and the apparent contact angle ϕ_D is measured at a distance ℓ_C from the contact line where ℓ_C denotes the capillary length.

minimal fluid volumes, and can be performed with easily accessible equipment. However, optical measurements may produce inconsistent results as the techniques are sensitive to local surface imperfections, optical obstructions, and subjective interface fitting [18]. At extreme contact angles ($<20^\circ$), optical contact angle measurement may not even be possible as fluid interfaces may not be discernible. Currently optical methods are the most widely used measurement technique. Force based methods such as the Wilhelmy plate [19], du Nouy ring [20], or capillary tube [18] indirectly measure the contact angle using a balance of forces and the Young's equation [21]. In comparison to optical methods, force based methods utilize quantities like contact line length or plate weight which can be objectively measured with a high degree of accuracy. Furthermore, these are averaged quantities as the force measurements are summed over the entire length of the contact line. While force based measurements of static contact angles can take advantage of high precision force sensors and objective measurements, they require a thoroughly validated model like the Young's equation.

Optical contact angle measurement techniques are easily applied to MCLs and thus they are still frequently used to measure dynamic contact angles [22–25]. However, the MCL is a multiscale problem [17] and the dynamic contact angle exhibits a dependence on the distance from the contact line; see Fig. 1. Following the definitions proposed by Cox [14], there exists a microscopic contact angle (ϕ_0) measured at a distance ϵ from the contact line and an apparent contact angle (ϕ_D) measured at a distance ℓ_C from the contact line; typically, ℓ_C is regarded as the capillary length scale. While optical contact angle measurements have been obtained at length scales as small as 10^{-5}m [26], the inner length scale is typically expected to be on the order of 10^{-7}–10^{-9}m and thus inner contact angles are typically obtained by extrapolation of the interface. Force based methods have been implemented successfully at low Capillary numbers [27–29], but have shown inconsistent contact angle measurements at larger Capillary numbers [30]. This is partly due to poor estimations of additional forces like viscous drag [31]. In this work we will revisit the dynamic Wilhelmy plate experiment with a goal of quantitatively determining the effect of viscous drag forces. To achieve this objective we will use particle image velocimetry to experimentally measure the velocity field and shear stress along the Wilhelmy plate and evaluate preexisting drag force models. It will be shown that preexisting models do not accurately capture the effect of the interface curvature, the plate tip, or the finite size of the fluid container so that they underestimate the shear stress and viscous drag. Therefore, we develop a new model that incorporates the apparent contact angle, flow around the leading edge of a flat plate, and size of the fluid container. This viscous drag model is

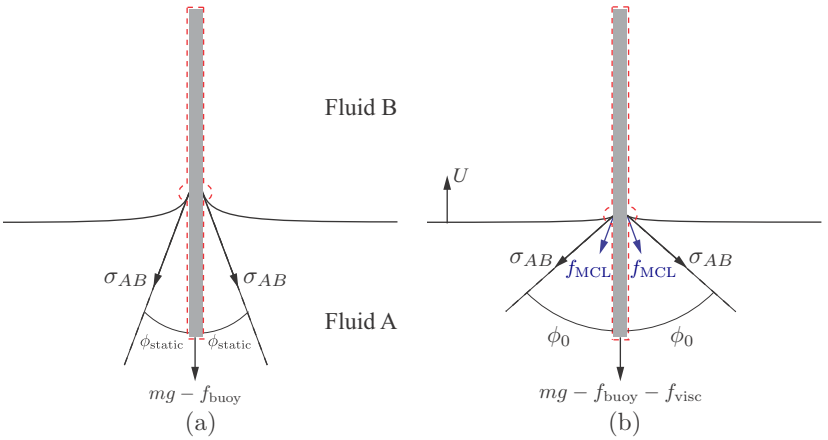

FIG. 2. Schematic of the control volume and forces acting on (a) static Wilhelmy plate and (b) dynamic Wilhelmy plate. The dashed red line defines the control volume over which the forces are summed. ϕ_{static} denotes the static contact angle and ϕ_0 denotes the dynamic microscopic contact angle. Schematic is not drawn to scale.

validated against PIV measurements and subsequently used to obtain high accuracy measurements of the dynamic contact angle.

This paper is organized as follows. Section II will review the theoretical foundations of the static Wilhelmy plate method and extend the method to moving contact lines. Section III provides the details of our experimental setup, which includes the fluid properties, Wilhelmy plate apparatus, and configuration for particle image velocimetry. Section IV presents viscous drag force measurements, examines preexisting models, and proposes a new drag force model. This new viscous drag model is applied in Sec. V to obtain measurements of the microscopic dynamic contact angle and concluding remarks are found in Sec. VI.

II. THEORETICAL FOUNDATIONS OF THE STATIC AND DYNAMIC WILHELMY PLATE EXPERIMENT

The static Wilhelmy plate [19] is an experimental method based on the Young's equation and designed to measure the static contact angle using a partially submerged thin plate. As seen in Fig. 2(a), the total force which acts in the vertical direction on the control volume enclosed by the dashed red line is given by

$$f_{\text{total}} = P\sigma_{AB}\cos(\phi_{\text{static}}) + mg - f_{\text{buoy}}. \tag{1}$$

P is the perimeter of the plate or the length of the contact line, σ_{AB} is the surface tension between fluid A and B, ϕ_{static} is the static contact angle, m is the mass of the enclosed volume, g is gravity, and f_{buoy} is the buoyancy force. By measuring the total force acting on the enclosed volume, the static contact angle can be determined via Eq. (1). Force measurements can typically be obtained with a high degree of accuracy and thus the Wilhelmy plate method is commonly considered a reliable technique for static contact angle measurement [18]. Note that the dashed red line defines a control volume that encloses the solid plate and a small semicircular region around the MCL. The semicircular region has an infinitesimal radius ϵ and the boundary of the control volume lies in the fluid but arbitrarily close to the plate so that the mass of the enclosed liquid is negligibly small. The control volume depicted here is similar to the one proposed by Ramé [31] and provides an explanation as to why fluid-solid surface tension forces are absent from Eq. (1) [32].

TABLE I. Viscous drag force models proposed for the dynamic Wilhelmy plate experiment.

	Shear stress	Viscous drag force
Wang *et al.* [30]	$\tau = \dfrac{\mu U\left(R^2 - R_{\text{eq}}^2\right)}{R_{\text{eq}}\left[\left(R_{\text{eq}}^2 + R^2\right)\ln(R/R_{\text{eq}}) + R_{\text{eq}}^2 - R^2\right]}$	$f_{\text{visc}} = C_v \mu U \ell_D$
Karim and Kavehpour [37]	$\tau = \dfrac{4\mu U}{y\pi}$	$f_{\text{visc}} = \dfrac{4\mu U P}{\pi}\ln(\ell_D/\epsilon)$
Ramé [31]	$\tau = \dfrac{4\mu U}{\pi}\dfrac{\ell_D}{y\sqrt{\ell_D^2 - y^2}}$	$f_{\text{visc}} = \dfrac{4\mu U P}{\pi}\ln\left(\dfrac{\sqrt{\ell_D^2 - \epsilon^2} + \ell_D}{\epsilon}\right)$

The static Wilhelmy plate method can be extended to MCLs by inducing a constant interface velocity, U, so that the total force acting in the vertical direction on the control volume depicted in Fig. 2(b) is given by

$$f_{\text{total}} = P\sigma_{AB}\cos(\phi_0) + mg - f_{\text{buoy}} + f_{\text{MCL}} - f_{\text{visc}}. \tag{2}$$

f_{MCL} is the force of the moving contact line, also known as the unbalanced Young's force, and is given by

$$f_{\text{MCL}} = \sigma_{AB}[\cos(\phi_0) - \cos(\phi_{\text{static}})]. \tag{3}$$

f_{visc} is the viscous drag force acting over the surface of the submerged plate. In the following subsection, we present previous treatments of the viscous drag force.

Viscous drag force

In some dynamic Wilhelmy plate experiments, the viscous drag force is justifiably ignored at small Capillary numbers (Ca) [33–36]. However, the drag force has been identified as a source of error in dynamic Wilhelmy plate experiments at moderate to high Ca [30]. In experiments where viscous drag forces cannot be ignored, three models have been proposed by Wang *et al.* [30], Karim and Kavehopour [37], and Ramé [31] and are listed in Table I. These viscous drag models have been rewritten to be consistent with the coordinate system and variables shown in Fig. 3.

Wang *et al.* suggested that the viscous drag force acting on a Wilhelmy plate could be modeled by the parallel motion of a cylinder of radius R_{eq} inside a larger cylinder of radius R. Assuming infinitely long cylinders, they obtained an analytic relation for shear stress that scales with μU, depends on the container size $(R^2 - R_{\text{eq}}^2)$, and is independent of the submerged depth ℓ_D. In determining the viscous drag force, Wang *et al.* encapsulated the effects of R and R_{eq} into a drag coefficient C_v to be fitted using experimental results.

Karim and Kavehpour suggested that the shear stress along the plate is dominated by the effects of the MCL. Assuming a perfectly flat interface, the authors reported a shear stress that is identical to Huh and Scriven's [38] solution for $\phi_0 = 90^\circ$ so that the shear stress scales as $1/y$ where y denotes the distance from the contact line. Using a cut-off length scale ϵ, Karim and Kavehpour integrated this shear stress to obtain the viscous drag force shown in row two of Table I.

The most detailed viscous drag model was proposed by Ramé [31] who extended a solution first reported by Garabedian [39] to analytically determine the Stokes flow around a finite-length plate plunging into an infinite fluid bath. Ramé's solution relied on symmetry boundary conditions and thus his model also assumes a flat interface that intersects the Wilhelmy plate at 90°. As seen in Table I, the shear stress model proposed by Ramé diverges as $1/y$ in the limit of $y \to 0$ and diverges as $1/\sqrt{\ell_D^2 - y^2}$ in the limit of $y \to \ell_D$ where ℓ_D is the submerged depth. These divergent stresses are generated by the geometric MCL and plate tip singularity, respectively. Using a microscopic cut off length scale ϵ when integrating Ramé's proposed shear stress profile yields the viscous drag force shown in row three of Table I. If ϵ is small so that $\sqrt{\ell_D^2 - \epsilon^2} \approx \ell_D$, then the viscous drag force is

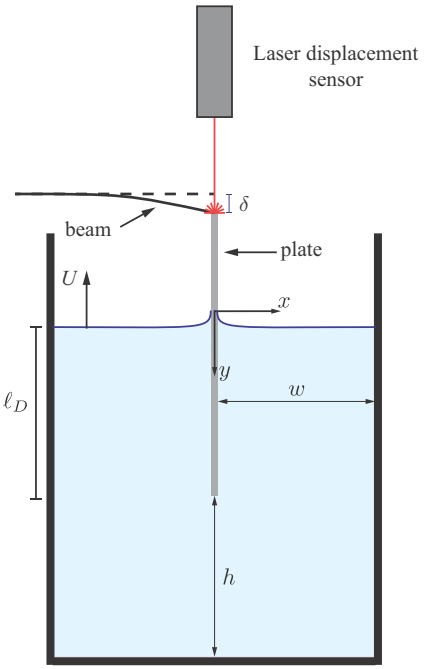

FIG. 3. Schematic of the dynamic Wilhelmy plate experiment using an elastic beam and displacement sensor to measure forces. ℓ_D denotes the submerged depth of the plate, δ is the deflection the beam tip, w is the distance between the plate and edges of the fluid container, and h is the distance between the plate and the bottom of the fluid container.

approximated by

$$f_{\text{visc}} \approx \frac{4\mu U P}{\pi}\left[\ln\left(\frac{\ell_D}{\epsilon}\right) + \ln(2)\right]. \tag{4}$$

The drag force predicted by Ramé exhibits the same logarithmic dependency on the submerged depth as Karim and Kavehpour's model but is greater in magnitude due to the additional force contribution of the plate tip.

The viscous drag forces predicted by these three models are distinctly different and it is unclear which model is best suited for the Wilhelmy plate method as there is no published experimental validation to the best of our knowledge. Therefore, we will use particle image velocimetry (PIV) [40] to measure the flow around the dynamic Wilhelmy plate. In the sections below, we will find that existing models do not fully capture the shear stress profile and thus we will develop a new model.

III. EXPERIMENTAL SET-UP AND VALIDATION

In this work a dynamic Wilhelmy plate experiment was constructed to measure the viscous drag force, the force of the MCL, and the microscopic dynamic contact angle. To achieve this goal we required an apparatus capable of force measurements on the order of 10^{-4}–10^{-5} N, controlled contact line motion, and PIV measurements. As depicted in Figs. 3 and 4, the Wilhlemy plate was suspended from a thin elastic beam whose deflection was measured using a Keyence LK-H027 laser displacement sensor. Following beam bending theory, the deflection of the beam will be linearly correlated to the force applied at the tip. The displacement sensor has a resolution of

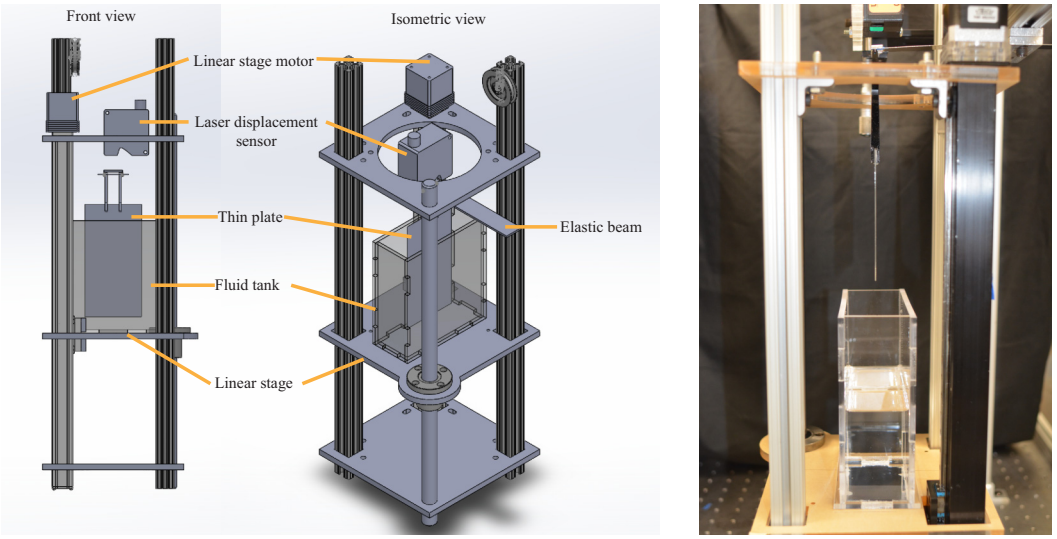

FIG. 4. (a) Schematic of the vertical stage used to raise and lower the fluid tank. (b) Picture of vertical stage, fluid container, and plate used in the Wilhelmy plate experiment.

0.02 μm, collects measurements at 250 Hz, and uses a low pass filter with a cutoff frequency of 30 Hz. An adjustable beam length coupled with a high resolution displacement sensor yields a sensitive and adaptable force sensor that can be calibrated with a set of known weights. To induce contact line motion, a rectangular tank containing glycerin is placed on a vertical stage driven by a Pololu SY42STH38 motor controlled via an Arduino. The tank has internal dimensions of $5.5\times15\times25$ cm^3. In this configuration the vertical stage is capable of smoothly accelerating to and translating at velocities of 0.1–11 mm/s. To minimize any force measurement errors, the laser displacement sensor is independently mounted to a Newport RS 1000 vibration damped optical table. The glycerin is contained in a transparent acrylic tank to allow transmission of laser light for PIV measurements. A laser sheet is generated from a 200 mJ Nd:YAG laser (New Wave Solo XT, $\lambda = 532$ nm) and illuminates 20 μm seeding particles. Images are captured using a Sigma 24–70 mm lens attached to a Powerview Plus 630159 camera with 2048×2048 pixels^2. The captured images have an approximate spatial resolution of 40 μm per pixel and are processed using TSI Insight 4G software. The entire experiment resides inside an enclosure to minimize contaminants and fluctuations in temperature and humidity.

A. Fluid and solid properties

In this experiment the fluid and solid were selected to be Evonik 99% pure glycerin and Corning gorilla glass. The glass plate has a thickness of 0.55 mm and a height and width of 100 mm. The glass plate was chosen for its chemical resistance and ability to pass laser light so that PIV measurements can be obtained near the plate surface. Glycerin was chosen for its high viscosity and small static contact angle as these properties are expected to have more measurable changes in microscopic contact angle and moving contact line forces. The properties of the glycerin are reported in Table II and were obtained from the measurements using a cannon-fenske capillary viscometer, a high-precision scale, and static Wilhelmy plate measurements. All fluid properties were found to be within 5% of the values reported by Cheng [41] and Takamura *et al.* [42].

TABLE II. Fluid properties of glycerin on a glass substrate.

ν, Kinematic viscosity	1.03×10^{-3} m^2/s
ρ, Density	1262 kg/m^3
μ, Dynamic viscosity	1.302 Ns/m^2
$\phi_{\text{static,adv}}$, Static advancing contact angle	$44^\circ \pm 3^\circ$
$\phi_{\text{static,rec}}$, Static receding contact angle	$82^\circ \pm 3^\circ$
σ, Surface tension	0.064 N/m

B. Calibration and validation

The force sensor is calibrated by suspending a set of known weights from the tip of the beam and measuring the displacement. The beam deflection varies linearly with respect to the force applied and has confidence bounds of approximately $\pm5\times10^{-5}$ N for static measurements [43]. The Wilhelmy plate setup was validated by measuring the static contact angle for deionized water via force measurements and comparing the results to optical measurements. Optical contact angle measurements were obtained by converting the images to grayscale, identifying the interface, and fitting an exponential function to the interfacial points. Images of the contact line, Fig. 5, show an angle of $46^\circ \pm 3^\circ$ while force-based measurements yield a static advancing contact angle of $44^\circ \pm 3^\circ$. In this work we only consider advancing contact lines and will therefore only use the static advancing contact angle. After validating the setup with water, the static Wilhelmy plate experiment was used to measure the surface tension of glycerin.

C. Experimental procedure

For each experimental measurement of microscopic contact angle we conducted 20 independent advancing contact line tests. The first 10 tests measure the drag force acting on the plate using a container of glycerin that has been seeded with PIV particles. PIV images are captured at a frequency ranging from 3.5 to 7.25 Hz where the frequency is chosen so that there is at least one PIV image pair for every millimeter of interface travel. The PIV measurements are conducted separately to ensure that force measurements are not affected by any PIV particles that may cluster near the interface or contact line. The time delay between PIV image pairs is adjusted between 0.032 and 0.12 seconds to ensure an optimal particle displacement of roughly 10 pixels. An iterative multipass evaluation algorithm is performed on each image pair starting from a 40×40 pixel^2 interrogation window to a 20×20 pixel^2 window resulting in a spatial resolution of 0.4 mm. The PIV velocity measurements are ensemble averaged across ten tests so that the measurement uncertainty, defined as twice the standard deviation, is approximately 1.8×10^{-4} m/s. Between each individual test the glass plate is

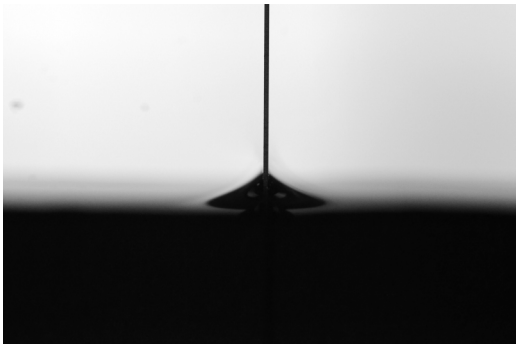

FIG. 5. Image of the static water-air interface used to validate the static Wilhelmy plate experiment.

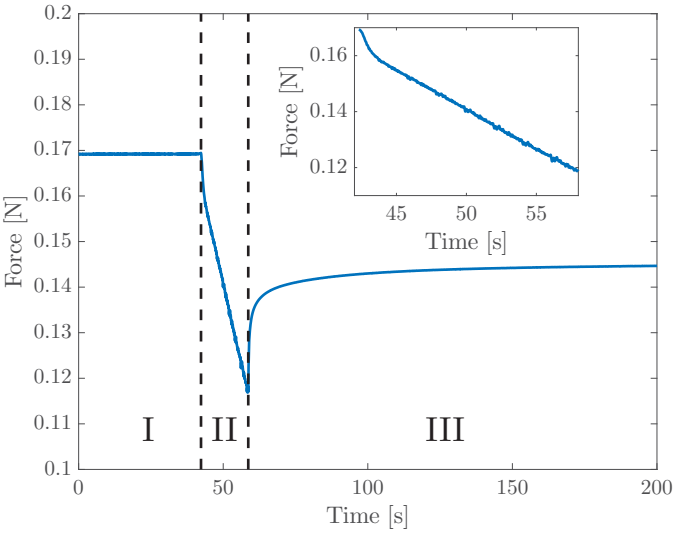

FIG. 6. Measured force vs. time for a contact line advancing at 5 mm/s. In region I the plate is statically suspended above the fluid. The fluid interface makes contact with the plate at the start of region II, advances up the surface of the plate, and is impulsively stopped at the end of region II. In region III the contact line relaxes to its static shape. Inset shows a magnified view of region II.

cleaned with acetone, rinsed with deionized water, and dried. A second set of 10 tests are performed with no PIV particles to measure the total force acting on the plate and a representative example of the force over a single test is shown in Fig. 6. In region I, the plate hangs freely from the elastic beam and lies above the surface of the fluid. Therefore the force measured in region I is the plate weight only. At time zero, the vertical stage accelerates to a constant velocity U. At the beginning of region II the fluid interface makes contact with the plate tip. Inside region II, the contact line advances along the plate and the total force decreases in magnitude as surface tension, viscous drag, and buoyancy forces act on the plate. At the end of region II the vertical stage is impulsively stopped and the experiment becomes a static Wilhelmy plate as the fluid motion settles and the contact line relaxes to its static shape.

IV. VISCOUS DRAG FORCE MODEL

Following the experimental procedure described in the previous section we obtain the velocity field shown in Fig. 7(a). This figure shows a typical result for an advancing interface and corresponds to an interface velocity of 7.5 mm/s in this particular case. The color contours depict the fluid stress normal to the plate surface ($\mu \partial v/\partial x$) and the shear stress along the plate surface ($x = 0$) is plotted in Fig. 7(b). v is the y component of velocity tangential to the plate surface. As expected, the stress diverges near the two geometric singularities of the problem, namely the MCL at $y = 0$ and the plate tip at $y = \ell_D \approx 0.041$. When compared to the models listed in Table I, it becomes clear that preexisting models do not capture the shear stress profile. These underestimations of shear stress and viscous drag subsequently affect measurements of the MCL force and dynamic contact angle. In the discussion below, we identify the sources of error in existing models and propose a new model for future dynamic Wilhelmy plate experiments.

Three primary regions are observed upon inspecting the PIV measurements in Fig. 7, namely, the MCL region, plate tip region, and an intermediate region. Near $y = 0$ the flow is dominated by the MCL so that shear stress scales as $1/y$ and diverges at a rate proportional to the apparent contact angle. Near $y = \ell_D$ the flow around the plate tip dominates and shear stress diverges at a rate that

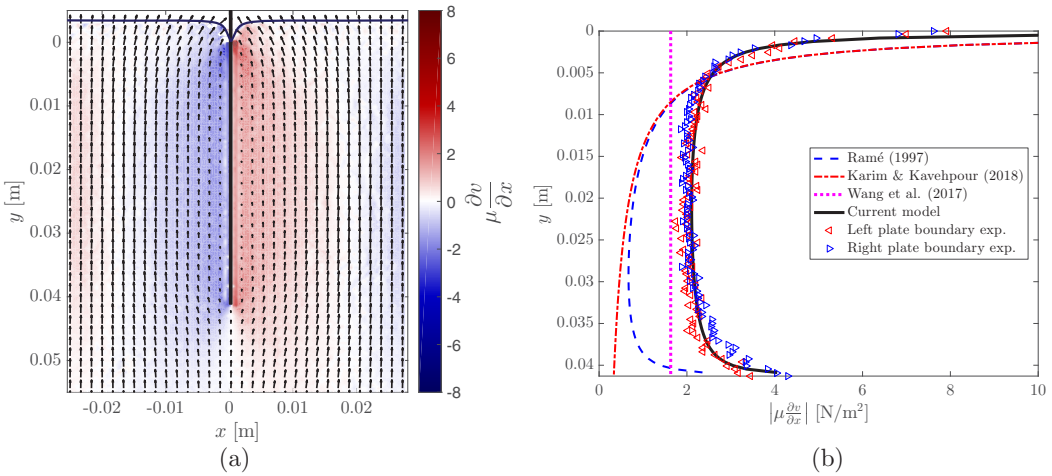

FIG. 7. (a) Velocity field and plate normal stress for glycerin advancing at 7.5 mm/s. The Wilhelmy plate and interface are denoted by the solid black lines. The contact line lies at $y = 0$. Only a quarter of the measured vectors have been plotted for clarity. (b) Comparison of theoretical and experimental shear stress along the plate surface. y denotes the distance from the the moving contact line.

is slower than that of the MCL. While the effects of the MCL and plate tip are strong near each respective singularity, their effects decay rapidly and the intermediate region reveals that there is a background flow that creates a constant shear stress along the plate. Wang *et al.* considers only the background flow and thus fails to capture the diverging stress at both the MCL and plate tip. Karim and Kavehpour assume a 90° contact angle and do not account for the plate tip or background flow so that their model diverges more quickly near the MCL and decays towards zero as distance from the MCL increases. Ramé's model assumes an infinite domain as well as a 90° contact angle and thus fails to capture the rate of divergence near the MCL and the region of constant shear stress in the intermediate region.

Recognizing the limitations of preexisting models, we observe that there are three regions where the shear stress is dominated by the MCL flow, background flow, and flow around the plate tip. In the small Reynolds number limit where the flow is linear, we can expand the stream function and shear stress associated with the flow around a Wilhelmy plate as

$$\psi = \psi_{\mathrm{MCL}} + \psi_{\mathrm{int}} + \psi_{\mathrm{tip}} + \psi_n, \tag{5}$$

$$\tau = \tau_{\mathrm{MCL}} + \tau_{\mathrm{int}} + \tau_{\mathrm{tip}} + \tau_n. \tag{6}$$

The first three terms correspond to the flows whose shear stresses are dominant in the MCL, intermediate, and plate tip region, while the last term represents the flow which is dominant far from the Wilhelmy plate and near the tank walls. Determining ψ_n and τ_n is not a trivial task however since we are only interested in the shear stress along the plate ($x = 0$), we take the leading-order approximation and only consider the first three terms. Comparisons with PIV measurements will show that these three terms are a good estimation of the shear stress along the surface of the submerged plate.

In the MCL region, the dominant characteristics of the flow are captured by the model proposed by Huh and Scriven [38]. For an arbitrary apparent contact angle, the shear stress in the outer region along the plate is given by

$$\tau_{\mathrm{MCL}} = \frac{2\mu U D_A}{y}, \tag{7}$$

where D_A is a dimensionless coefficient from Huh & Scriven's solution computed using the apparent contact angle [44]. In the plate tip region, the flow is largely unaffected by the MCL and is essentially a Stokes flow around the leading edge of a flat plate. The dominant term in this problem was reported by Carrier and Lin [45] and can be mapped to the Wilhelmy plate geometry so that the shear stress along the plate is given by

$$\tau_{\text{tip}} = \frac{\mu U}{\sqrt{h(\ell_D - y)}}. \tag{8}$$

Here h is the distance from the plate tip to the bottom of the fluid container as depicted in Fig. 3. In the intermediate region the background flow can be modeled as a Couette-Poiseuille flow where the velocity profile is given by

$$v = \frac{1}{2\mu}\frac{\partial p}{\partial y}x^2 + \left[\frac{U}{w} - \frac{w}{2\mu}\frac{\partial p}{\partial y}\right]x. \tag{9}$$

The shear stress along the plate boundary ($x = 0$) is given by

$$\tau_{\text{int}} = \frac{\mu U}{w} - \frac{w}{2}\frac{\partial p}{\partial y}. \tag{10}$$

w is the distance between the plate surface and tank wall while the pressure gradient, determined by conservation of mass, is given by

$$\frac{\partial p}{\partial y} = -\frac{6\mu U}{w^2}. \tag{11}$$

Combining these three terms yields the shear stress profile given by

$$\tau = \frac{2\mu U D_A}{y} + \frac{4\mu U}{w} + \frac{\mu U}{\sqrt{h(\ell_D - y)}}, \tag{12}$$

and the solid curve shown in Fig. 7(b) where an apparent contact angle of 135° is used to compute the value of D_A. The current model is in good agreement along the entire length of the submerged plate and captures the shear stress in all three regions. Additional comparisons are provided in Fig. 8 where the Couette-Poiseuille velocity profile and shear stress at different depths are validated. At shallow depths the current model slightly underestimates the shear stress suggesting that terms from τ_n may become significant in the limit of $\ell_D \to 0$. For the purposes of the dynamic Wilhelmy plate experiment, we can avoid this small error by simply using measurements where ℓ_D is large. If we nondimensionalize the shear stress by σ_{AB}/ℓ_D to obtain

$$\frac{\tau}{\sigma_{AB}/\ell_D} = 2\text{Ca}D_A\frac{\ell_D}{y} + 4\text{Ca}\frac{\ell_D}{w} + \text{Ca}\sqrt{\frac{\ell_D}{h}\frac{\ell_D}{\ell_D - y}}, \tag{13}$$

we observe that the stress scales with Ca as expected but also exhibits a dependence on several length-scale ratios which highlight the relative importance of each term. As one expects, the MCL and plate tip terms containing ℓ_D/y and $\ell_D/(\ell_D - y)$ will dominate in the limit of $y \to 0$ and $y \to \ell_D$, respectively. The length-scale ratios ℓ_d/w and ℓ_d/h represent the size of the plate relative to the fluid container and indicate that the intermediate and plate tip terms will become more important as the size of the container decreases.

Given the match in shear stress profiles, we integrate along the length of the submerged plate to obtain the viscous drag force given by

$$f_{\text{visc}} = P\int_{\epsilon}^{\ell_D} \tau dy = 2\mu U P D_A \ln\left(\frac{\ell_D}{\epsilon}\right) + 4\mu U P\frac{\ell_D - \epsilon}{w} + 2\mu U P\sqrt{\frac{\ell_D - \epsilon}{h}}. \tag{14}$$

This new model of viscous drag incorporates the effects of apparent contact angle, the plate tip, and a finite-sized domain. The coefficient D_A is dependent on the apparent contact angle and thus dictates

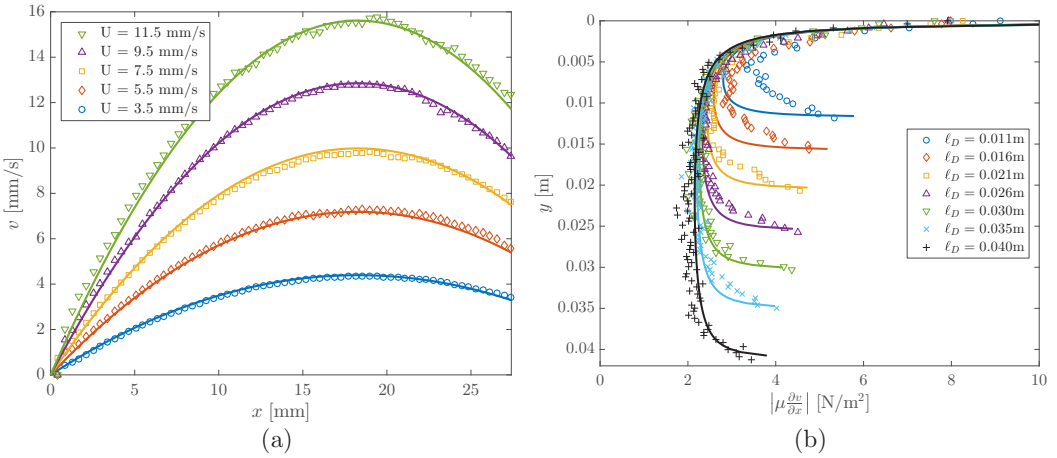

FIG. 8. Validation of the current viscous drag force model. Markers denote experimental PIV measurements and solid lines denote the current model. (a) Comparison of the vertical velocity profile in the intermediate region ($y = \ell_D/2$) for various contact line velocities. Theoretical velocity profiles are determined using Eq. (9). (b) Comparison of the shear stress profile at various plate depths for an interface velocity of 7.5 mm/s. Theoretical shear stress profiles are determined using Eq. (12).

the rate of divergence near $y = 0$. In the limiting case where the apparent contact angle is equal to 90°, $D_A = 2/\pi$ and the current model diverges at the same rate as Ramé's model and Karim and Kavehpour's model. The current model diverges as $1/\sqrt{\ell_D - y}$ as $y \to \ell_D$ and captures the relatively slower divergence in stress (when compared to the divergence in stress near the MCL). Stress in the current model diverges slightly faster than Ramé's model, which diverges as $1/\sqrt{\ell_D^2 - y^2}$; however, it is difficult to distinguish which model is more accurate based on the experimental data as these two rates are similar. Last, the current model captures the constant shear stress generated by the background flow and indicates that it is dependent on the finite size of the fluid tank via the parameter w. Overall preexisting models underestimate the magnitude of the shear stress so that when ϵ is treated as a free parameter, it must take on smaller values to obtain reasonable viscous drag forces. This may lead to confusion as ϵ is sometimes interpreted as an estimation of the slip length and thus highlights the importance of accurate drag force modeling.

Based on the current model, we can also identify the regimes in which it is reasonable to neglect viscous drag by examining the ratio of the viscous force to the surface tension force, i.e.,

$$\frac{f_{\text{visc}}}{P\sigma_{AB}\cos(\phi_0)} = \frac{\text{Ca}}{\cos(\phi_0)}\left[2D_A \ln\left(\frac{\ell_D}{\epsilon}\right) + 4\left(\frac{\ell_D}{w} - \frac{\epsilon}{w}\right) + 2\sqrt{\frac{\ell_D}{h} - \frac{\epsilon}{h}}\right]. \tag{15}$$

Viscous drag forces cannot be neglected if this ratio is of order one or greater. At first glance this ratio scales as Ca as one expects but also shows a dependence on the contact angle and the size of the container. If the contact angle is 90°, then there is zero surface tension force acting tangential to the plate and a viscous force of any magnitude will affect the dynamic contact angle measurement. Even at contact angles not equal to 90°, $\cos(\phi_0)$ is always less than one and thus viscous forces may be significant for Ca < 1. Inside the square brackets of Eq. (15), geometry dependent parameters such as ℓ_D/w and ℓ_D/h appear indicating that larger fluid containers will reduce the effect of viscous drag. In many applications large volumes of fluid are not always practical and thus the current model provides a way to account for the viscous drag effect in relatively small containers. In future works this ratio can be used to design dynamic Wilhelmy plate experiments or to better understand previous Wilhelmy plate results. In the following section, we briefly demonstrate the practical application

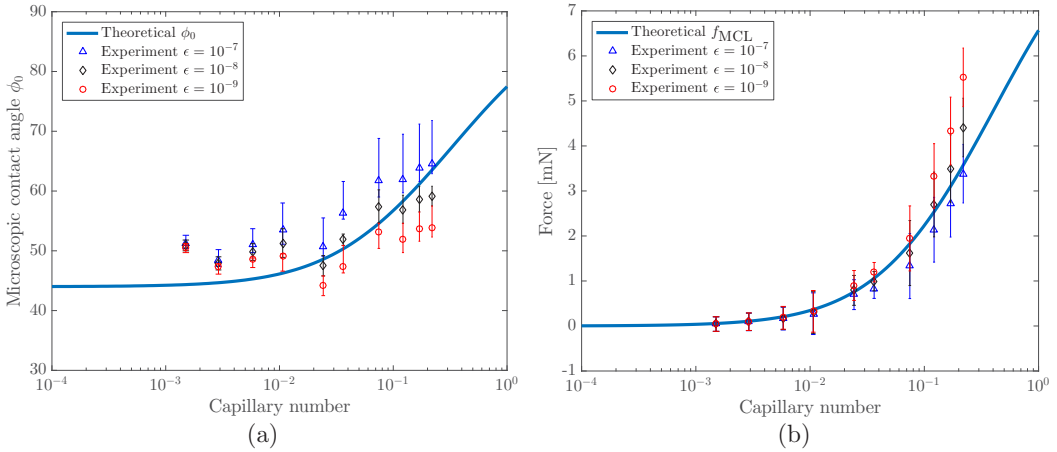

FIG. 9. (a) Microscopic dynamic contact angle and (b) force of the moving contact line measured by the dynamic Wilhelmy experiment for glycerin advancing over a glass substrate. Theoretical contact angles and moving contact line forces are modeled by the dynamic Young's equation presented in Eq. (16), which was originally proposed in our previous publication [46].

of the viscous drag force model and measure the microscopic contact angle and MCL force in a dynamic Wilhelmy plate experiment.

V. DYNAMIC MICROSCOPIC CONTACT ANGLE AND MOVING CONTACT LINE FORCE

For this Wilhelmy plate experiment, tests were conducted at 0.1–11 mm/s where the total force, plate weight, and buoyancy force were directly measured. Estimating the viscous drag force using the model developed in the previous section, we obtain the microscopic contact angle measurements and MCL forces shown in Fig. 9. The results are consistent with the dynamic Young's equation proposed in our previous work [46] and given by

$$2\phi_0\mu_A UC_A + 2(\pi - \phi_0)\mu_B UC_B - \sigma_{AB}\cos(\phi_0) = \sigma_{AS} - \sigma_{BS}, \tag{16}$$

where C_A and C_B are coefficients from Huh and Scrivens solution [38,47]. The dynamic Young's equation is an extension of the static Young's equation to a moving contact line in which viscous forces balance surface tension forces. In our previous work, we recognized that the contact line is defined by the intersection of three fluid interfaces and that one must account for the forces acting along each to capture the total force of the MCL. Therefore, we integrated the stress predicted by Huh and Scriven's solution over a control volume enclosing all three interfaces and demonstrated that the stress singularity is integrable and that there is a finite viscous force which acts at the MCL. The balance of this viscous force with surface tension yields the dynamic Young's equation and indicates that the microscopic contact angle is a function of the Capillary number. The dynamic Young's equation is consistent with diffuse interface models [48–50] and molecular kinetic models [17,51,52], which also report that microscopic contact angle is dependent on the Capillary number. The advantage of the dynamic Young's equation is that it only depends on macroscopic parameters that can be measured independently.

The experimental results show that in the limit of $\mathrm{Ca} \to 0$, the microscopic dynamic contact angle approaches the static contact angle. As Ca increases from approximately 10^{-3} to 10^{-1} we observe an increase in contact angle by approximately 20° and a corresponding increase in the moving contact line force. These results indicate that the constant microscopic contact angle assumption made by Cox [14], Voinov [15], and others is reasonable in the limit of $\mathrm{Ca} \to 0$. The

results are also consistent with the observations made by Ramé [26] and others [53,54] who have reported increases in microscopic contact angles as Ca $\rightarrow$ 1.

In Fig. 9, the results are plotted for $\epsilon = 10^{-7}, 10^{-8}$, and 10^{-9}m. At small Ca the force measurements are not sensitive to ϵ because the total viscous drag force itself is not significant. As Ca increases, the value of ϵ that best matches the theory increases from 10^{-9}m to 10^{-7}m. As ϵ is defined as the length over which slip occurs, this result is consistent with molecular dynamics simulations that report increasing fluid slip at larger Capillary numbers. If ϵ is of the same order of magnitude as slip, as suggested by Cox [14], then the values of ϵ reported here are consistent with the glycerin-glass slip lengths reported by Cottin-Bizonne *et al.* [55]. We note that measurements of contact angle are somewhat sensitive to uncertainty in MCL force measurements. Taking the derivative of Eq. (3) yields

$$\frac{\partial \phi_0}{\partial f_{\mathrm{MCL}}} = -\frac{1}{P\sigma_{AB}\sin(\phi_0)}. \tag{17}$$

It can be seen that smaller contact line lengths or surface tensions will result in more sensitivity to measurement error. In the current experiment, the sensitivity of the contact angle measurement is roughly 6°/mN. While the measured change in microscopic contact angle appears relatively small, it could have a significant impact on a variety of wetting phenomena such as air entrainment at an advancing contact line [17]. In a recent work by Kamal *et al.* [56], the critical Capillary number marking the onset of air entrainment was correlated to the force acting at the MCL and the microscopic contact angle. The authors noted that the critical Capillary number could change by up to 0.6 over a 20° range, i.e. the same range of angles observed in our present experiment.

VI. CONCLUDING REMARKS

In this work we revisited the dynamic Wilhelmy plate experiment to measure and model the viscous drag force acting along the submerged surface of the plate. PIV measurements revealed that viscous drag forces can be of the same order of magnitude as surface tension forces and if ignored, will induce errors in dynamic contact angle measurement. Preexisting models were found to underestimate this force due assumptions that either ignore the interface curvature, the tip of the Wilhelmy plate, or the flow generated between the plate and fluid container. Recognizing that poor estimations of the viscous drag force will affect contact angle measurements, we proposed a new viscous drag force model that incorporates the effects of the MCL, the leading edge of a flat plate, and a Couette-Poiseuille flow. This new viscous drag force model was found to be in good agreement with PIV measurements for $0.001 < \mathrm{Ca} < 0.3$. The performance of the model did not degrade at higher velocities and suggests that the model could be applied at even higher Ca. When compared to surface tension forces, viscous drag forces were found to be significant if Ca is the same order of magnitude as $1/\cos(\phi_0)$ or if the the separation between the plate and fluid container are small. As a demonstrative example, the proposed drag force model was used to measure microscopic contact angles and MCL forces for glycerin advancing over a glass substrate. Measurements of the microscopic contact angles show a 20° increase as Ca varies from 10^{-3} to 10^{-1} and is in agreement with the dynamic Young's equation proposed in our previous work [46]. Measurements of the MCL force also showed that the Wilhelmy plate method is insensitive to the inner length scale ϵ in the limit of Ca $\rightarrow$ 0. Based on the present results, the dynamic Wilhelmy plate method can be more confidently applied to measure dynamic contact angles.

ACKNOWLEDGMENTS

We acknowledge the Office of Naval Research for their support in this research effort. We also acknowledge Dr. Adam C. DeVoria for his helpful discussions and comments.

[1] A. L. Yarin, Drop impact dynamics: Splashing, spreading, receding, bouncing..., Annu. Rev. Fluid Mech. **38**, 159 (2006).
[2] V. K. Dhir, Boiling heat transfer, Annu. Rev. Fluid Mech. **30**, 365 (1998).
[3] S. J. Weinstein and K. J. Ruschak, Coating flows, Annu. Rev. Fluid Mech. **36**, 29 (2004).
[4] B. Derby, Inkjet printing of functional and structural materials: Fluid property requirements, feature stability, and resolution, Annu. Rev. Mater. Res. **40**, 395 (2010).
[5] P.-G. de Gennes, Wetting: Statistics and dynamics, Rev. Mod. Phys. **57**, 827 (1985).
[6] L. Landau and B. Levich, Dragging of a liquid by a moving plate, in *Dynamics of Curved Fronts* (Elsevier, Amsterdam, 1988), pp. 141–153.
[7] E. Vandre, M. Carvalho, and S. Kumar, Characteristics of air entrainment during dynamic wetting failure along a planar substrate, J. Fluid Mech. **747**, 119 (2014).
[8] F. Mugele and J. C. Baret, Electrowetting: From basics to applications, J. Phys.: Condens. Matter **17**, R705 (2005).
[9] H. Gelderblom, O. Bloemen, and J. H. Snoeijer, Stokes flow near the contact line of an evaporating drop, J. Fluid Mech. **709**, 69 (2012).
[10] H. Gelderblom, H. A. Stone, and J. H. Snoeijer, Stokes flow in a drop evaporating from a liquid subphase, Phys. Fluids **25**, 102102 (2013).
[11] T. D. Blake and J. M. Haynes, Kinetics of liquid/liquid displacement, J. Colloid Interface Sci. **30**, 421 (1969).
[12] Y. D. Shikhmurzaev, Moving contact lines in liquid/liquid/solid systems, J. Fluid Mech. **334**, 211 (1997).
[13] Y. D. Shikhmurzaev, *Capillary Flows with Forming Interfaces* (CRC Press, Boca Raton, FL, 2007).
[14] R. G. Cox, The dynamics of the spreading of liquids on a solid surface. Part 1. Viscous flow, J. Fluid Mech. **168**, 169 (1986).
[15] O. V. Voinov, Hydrodynamics of wetting, Fluid Dyn. **11**, 714 (1976).
[16] E. B. Dussan, The moving contact line: The slip boundary condition, J. Fluid Mech. **77**, 665 (1976).
[17] J. H. Snoeijer and B. Andreotti, Moving contact lines: Scales, regimes, and dynamical transitions, Annu. Rev. Fluid Mech. **45**, 269 (2013).
[18] G. Bracco and B. Holst, *Surface Science Techniques* (Springer Science & Business Media, Berlin, 2013).
[19] L. A. Wilhelmy, Wilhelmy plate method, Ann. Phys. **195**, 177 (1863).
[20] P. L. Du Nouy, An interfacial tensiometer for universal use, J. Gen. Physiol. **7**, 625 (1925).
[21] T. Young, An essay on the cohesion of fluids, Philos. Trans. R. Soc. London **95**, 65 (1805).
[22] R. L. Hoffman, A study of the advancing interface. I. Interface shape in liquid-gas systems, J. Colloid Interface Sci. **50**, 228 (1975).
[23] T. D. Blake and Y. D. Shikhmurzaev, Dynamic wetting by liquids of different viscosity, J. Colloid Interface Sci. **253**, 196 (2002).
[24] S. I. Karakashev, C. M. Phan, and A. V. Nguyen, Effect of sodium dodecylbenzene sulfonate on the motion of three-phase contact lines on the wilhelmy plate surface, J. Colloid Interface Sci. **291**, 489 (2005).
[25] E. Ramé and S. Garoff, Microscopic and macroscopic dynamic interface shapes and the interpretation of dynamic contact angles, J. Colloid Interface Sci. **177**, 234 (1996).
[26] E. Ramé, S. Garoff, and K. R. Willson, Characterizing the microscopic physics near moving contact lines using dynamic contact angle data, Phys. Rev. E **70**, 031608 (2004).
[27] C. Wang, S. Nair, and K. J. Wynne, Wilhelmy balance characterization beyond contact angles: Differentiating leaching from nanosurface reorganization and optimizing surface modification, Polymer **116**, 565 (2017).
[28] R. G. Chaudhuri and S. Paria, Dynamic contact angles on PTFE surface by aqueous surfactant solution in the absence and presence of electrolytes, J. Colloid Interface Sci. **337**, 555 (2009).
[29] Q. Min, Y.-Y. Duan, X.-D. Wang, Z.-P. Liang, and C. Si, Does macroscopic flow geometry influence wetting dynamic? J. Colloid Interface Sci. **362**, 221 (2011).
[30] X. Wang, Q. Min, Z. Zhang, Y. Duan, Y. Zhang, and J. Zhai, Influence of head resistance force and viscous friction on dynamic contact angle measurement in Wilhelmy plate method, Colloids Surf. A **527**, 115 (2017).

[31] E. Ramé, The interpretation of dynamic contact angles measured by the Wilhelmy plate method, J. Colloid Interface Sci. **185**, 245 (1997).
[32] A. Marchand, J. H. Weijs, J. H. Snoeijer, and B. Andreotti, Why is surface tension a force parallel to the interface? Am. J. Phys. **79**, 999 (2011).
[33] A. Al-Shareef, P. Neogi, and B. Bai, Force based dynamic contact angles and wetting kinetics on a Wilhelmy plate, Chem. Eng. Sci. **99**, 113 (2013).
[34] J. Park, U. Pasaogullari, and L. Bonville, Wettability measurements of irregular shapes with Wilhelmy plate method, Appl. Surf. Sci. **427**, 273 (2018).
[35] S. R. Ranabothu, C. Karnezis, and L. L. Dai, Dynamic wetting: Hydrodynamic or molecular-kinetic? J. Colloid Interface Sci. **288**, 213 (2005).
[36] S. Moulinet, C. Guthmann, and E. Rolley, Dissipation in the dynamics of a moving contact line: Effect of the substrate disorder, Eur. Phys. J. B **37**, 127 (2004).
[37] A. M. Karim and H. P. Kavehpour, Effect of viscous force on dynamic contact angle measurement using Wilhelmy plate method, Colloids Surf. A **548**, 54 (2018).
[38] C. Huh and L. E. Scriven, Hydrodynamic model of steady movement of a solid/liquid/fluid contact line, J. Colloid Interface Sci. **35**, 85 (1971).
[39] P. R. Garabedian, Free boundary flows of a viscous liquid, Commun. Pure Appl. Math. **19**, 421 (1966).
[40] M. Raffel, C. E. Willert, and J. Kompenhans, *Particle Image Velocimetry* (Springer-Verlag, New York City, NY, 1998).
[41] N.-S. Cheng, Formula for the viscosity of a glycerol-water mixture, Ind. Eng. Chem. Res. **47**, 3285 (2008).
[42] K. Takamura, H. Fischer, and N. R. Morrow, Physical properties of aqueous glycerol solutions, J. Pet. Sci. Eng. **98**, 50 (2012).
[43] See Supplemental Material at http://link.aps.org/supplemental/10.1103/PhysRevFluids.4.084004 for the calibration curve.
[44] See Supplemental Material at http://link.aps.org/supplemental/10.1103/PhysRevFluids.4.084004 for the analytic expression of D_A .
[45] G. F. Carrier and C. C. Lin, On the nature of the boundary layer near the leading edge of a flat plate, Q. Appl. Math. **6**, 63 (1948).
[46] P. Zhang and K. Mohseni, Theoretical model of a finite force at the moving contact line [Intl. J. Multiph. Flow (to be published)], arXiv:1711.05653.
[47] See Supplemental Material at http://link.aps.org/supplemental/10.1103/PhysRevFluids.4.084004 for the analytic expression of C_A and C_B.
[48] T. Qian, X.-P. Wang, and P. Sheng, Molecular scale contact line hydrodynamics of immiscible flows, Phys. Rev. E **68**, 016306 (2003).
[49] T. Qian, X.-P. Wang, and P. Sheng, A variational approach to moving contact line hydrodynamics, J. Fluid Mech. **564**, 333 (2006).
[50] W. Ren and W. E, Boundary conditions for the moving contact line problem, Phys. Fluids **19**, 022101 (2007).
[51] T. D. Blake, The physics of moving wetting lines, J. Colloid Interface Sci. **299**, 1 (2006).
[52] T. D. Blake and J. De Coninck, Dynamics of wetting and kramers theory, Eur. Phys. J. Special Topics **197**, 249 (2011).
[53] C. Shen and D. W. Ruth, Experimental and numerical investigations of the interface profile close to a moving contact line, Phys. Fluids **10**, 789 (1998).
[54] P. Sheng and M. Zhou, Immiscible-fluid displacement: Contact-line dynamics and the velocity-dependent capillary pressure, Phys. Rev. A **45**, 5694 (1992).
[55] C. Cottin-Bizonne, S. Jurine, J. Baudry, J. Crassous, F. Restagno, and E. Charlaix, Nanorheology: An investigation of the boundary condition at hydrophobic and hydrophilic interfaces, Eur. Phys. J. E **9**, 47 (2002).
[56] C. Kamal, J. E. Sprittles, J. H. Snoeijer, and J. Eggers, Dynamic drying transition via free-surface cusps, J. Fluid Mech. **858**, 760 (2019).